Investigation of potential hybrid capacitor property of chelated N-Heterocyclic carbene Ruthenium(II) complex

M. Akkoç, E. Öz, S. Demirel, V. Dorcet, Thierry Roisnel, A. Bayri, Christian Bruneau, S. Altin, S. Yaşar, I. Özdemir

Investigation of Potential Hybrid Capacitor Property of Chelated *N*-Heterocyclic Carbene Ruthenium(II) Complex

Mitat Akkoç [a] , Erdinç Öz [b,c], Serkan Demirel[b,d], Vincent Dorcet [e], Thierry Roisnel[e], Ali Bayri[b], Christian Bruneau [e], Serdar Altın [b,*] , Sedat Yaşar [a,*], İsmail Özdemir [a]

[a] İnönü University, Faculty of Science and Art, Department of Chemistry, 44280, Malatya, Turkey

[b] İnönü University, Faculty of Science and Art, Department of Physics, 44280, Malatya, Turkey

[c] Ankara University, Institute of Accelerator Technologies, Ankara, 06830, Turkey

[d] National Defense University, Naval Petty Officer Vacational School, Yalova, Turkey

[e] Université de Rennes, UMR 6226: CNRS Sciences Chimiques de Rennes, 35042, France

Corresponding Authors: Sedat Yaşar, Tel:+904223773735, Fax:+904223410212, e-mail:sedat.yasar@inonu.edu.tr; Serdar Altın, serdar.altin@inonu.edu.tr

Keywords: Cyclic Voltametry of ruthenium(II), hybrid capasitor; *N*-heterocyclic carbene; ruthenium; chelate ligand; transfer hydrogenation

Abstract

The synthesis of chelated ruthenium(II) complex type Ru(η^6-HMB)(NHC)Cl (NHC=*N*-heterocyclic carbene, HMB=hexamethylbenzene) is presented. The ruthenium(II)-NHC complex **6** was obtained in good yield and was fully characterised by NMR spectroscopy, X-ray diffraction and HRMS analysis. Electrochemical analysis by cyclic voltammetry (CV) revealed reversible redox behaviour at the ruthenium centre in **6**. DFT studies and the catalytic activity of complex **6** on transfer hydrogenation reaction of aryl ketones are also presented. The potential hybrid capacitor applications of Ru-NHC complex is discussed and reported firstly in the literature. It was found that the highest performance was found at 20.1 F/g, which is a promising result for energy storage applications.

1. Introduction

N-heterocyclic carbenes (NHCs) have become a widely used as a class of complexes in different areas such as transition metal catalysis [1], organocatalysis [2], biochemistry and medicine [3]. They are seen as an alternative to phosphine ligands, although their σ-donor property is more pronounced. This pronounced σ-donor property of NHC leads to more stable different transition metal ions at the centre of the molecule in the catalytic reaction, which does not readily undergo ligand dissociation [4]. Metal-carbon (M-C) bond stability may always be useful for catalytic activity, as many complexes carrying flexible NHC ligands combined with the robust nature of the M-NHC bond have been successfully used in high temperature required catalytic reactions [5-8]. Examples of ruthenium complexes (numbered 1-5 as seen in Figure 1), produced by chelating NHCs bearing oxygen [9,10], phosphorous [11,12], allyl [13], sulphur [14] and nitrogen [15-26] moieties, have been used successfully as catalysts for the transfer hydrogenation reaction. Peris and coworkers reported on rhodium and ruthenium complexes derived from an NHC ligand functionalised with a pendant alcohol [27]. In our case, a bidentate NHC-Ru(II) complex with a tethered carboxylate group was obtained by transmetallation of silver(I)-NHC to ruthenium(II) in dry dichloromethane (DCM). According to studies conducted by Peris et al., such complexes are formed as a result of in situ oxidation of the alcohol group. The results we reported in this study are consistent with this comment that Peris and his colleagues have done.

Compared to other imidazole functionalised NHC complexes, benzimidazole based-functionalised NHC ruthenium (II) complexes are still merit [28]. As far as we know, complex **6** in Figure 1 is the first example of a benzimidazole-based carboxylate donor functionalised NHC ruthenium(II) complex.
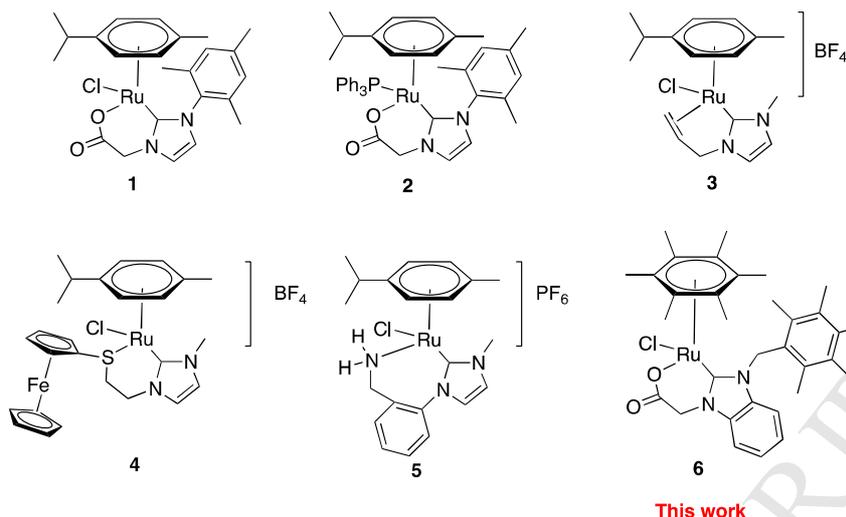
Figure 1. Some examples of bidentate chelating NHC-Ru(arene) complexes

In addition to the unique catalytic properties of *N*-heterocyclic carbenes, In addition to the catalytic activities of the NHCs, it is possible to have hybrid capacitor capability. Thus, they may be used on the energy storage devices . Hybrid capacitors consist of electrodes and electrolytes. In recent decades, hybrid capacitors have garnered considerable attention due to their intrinsic properties, i.e. a high capacity value of 4-250 Fg^{-1} [29]. It is well-known that a high capacity value of a hybrid capacitor can be achieved by the increasing the surface area and/or the conductivity of the electrodes [30]. Another important aspect of capacitors is to the search for new electrode materials. The highest capacitive performance of supercapacitors has been obtained with carbon-based materials [31]. Recently, studies have focused on metal oxide materials, i.e. Ni, Mn, Fe and Co, to achieve high capacitive performance [32]. Organic materials are another group of capacitors used in different devices such as poly(3,4-ethylenedioxythiophene) and poly(methyl methacrylate) [33]. Although organometallic complexes may consider as possible electrode materials for a device, there is no information about their capacitive performance.

The electrolyte materials are another important component of hybrid capacitors, as it is well-known that the capacity value changes from one electrolyte to another. For example, if the

electrolyte is changed from 1-ethyl-3-methylimidazolium bis(trifluoromethylsulphonyl)imide to H_2SO_4, the capacity of the cell increases from 65-150 Fg^{-1} to 454-710 Fg^{-1} [34].

Our group has been interested in the chemistry and catalytic activity of functionalised *N*-heterocyclic carbene and related transition metal complexes since the early 1990s. The study reported here describes the preparation of a redox-active benzimidazole-based oxygen donor NHC-ruthenium complex, which was assessed in the context of DFT, the catalytic activity during the transfer hydrogenation reaction and hybrid capacitor applications.

2. Results and Discussion

2.1.Synthesis and characterisation

The *N*-heterocyclic carbene precursor has been synthesized by addition of 2-iodoethanol to a *n*-BuOH solution of 1-(pentamethylbenzyl)benzimidazole at room temperature. Then the reaction mixture was heated and stirred at 120 °C for 24 h. This residue was purified to obtain 1-pentamethylbenzyl-3-hydroxyethylbenzimidazolium iodide salt as yellow crystalline solid. This salt soluble in water, methanol, acetonitrile, chlorinated solvents and DMSO. The resonance of the NC*H*N proton of 1-pentamethylbenzyl-3-hydroxyethylbenzimidazolium iodide salt in ¹H NMR (DMSO-d⁶⁾) observed at 8.97 ppm and NC*H*N carbons resonate in the ¹³C{¹H} NMR spectra at 141.8 ppm (see supporting information for NMR spectra).
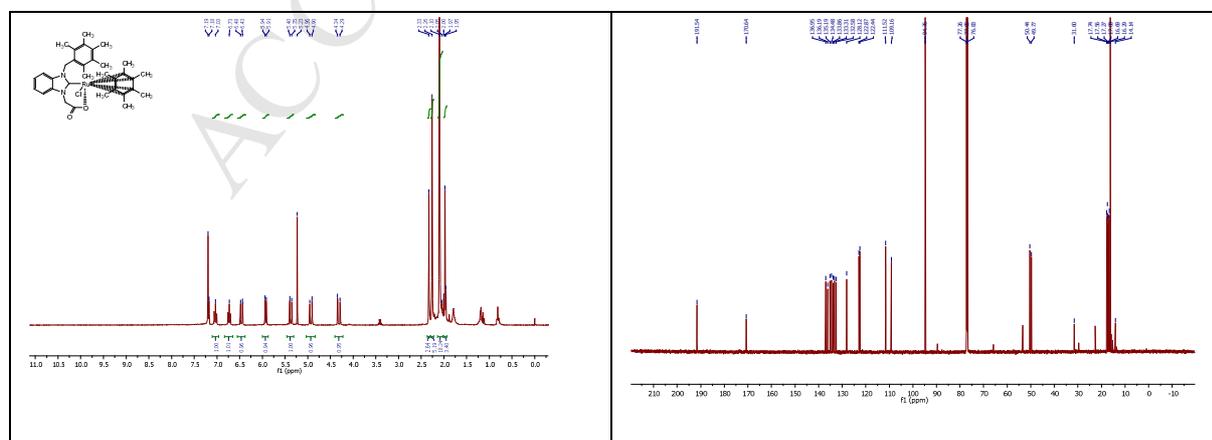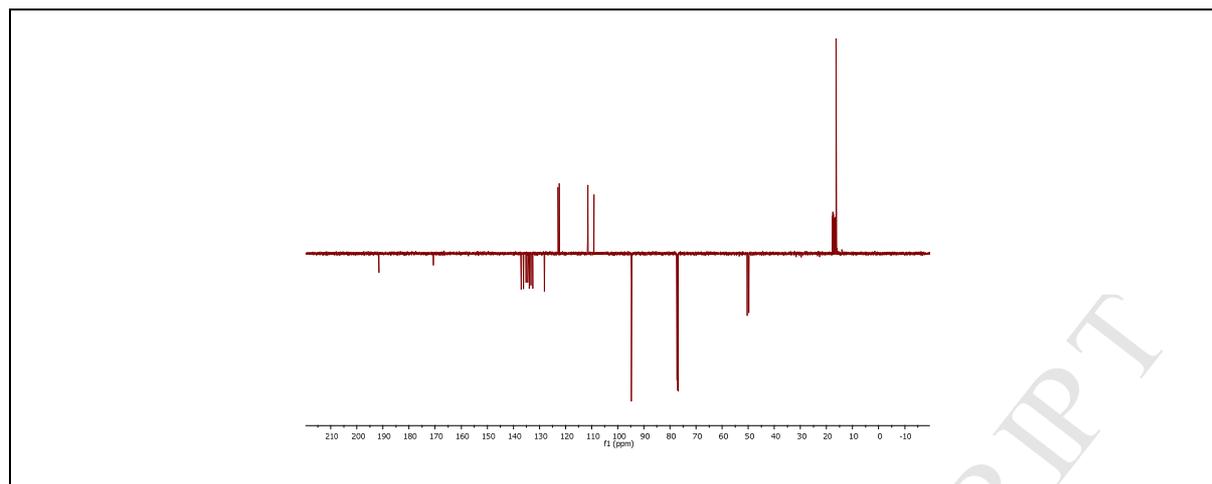
Figure 2 ^{1}H, ^{13}C and APT NMR spectra of complex **6**

Water soluble benzimidazolium salt was completely transformed into silver-NHC complex under *in situ* conditions by Ag_2O. To synthesis Ag(I)-NHC complex, Ag_2O (1 mmol), 1-pentamethylbenzyl-3-hydroxyethylbenzimidazolium iodide salt (1 mmol) and 20 mL dry DCM was put in to a Schlenk tube under argon and stirred 24 hours under exclusive of light. The Ag(I)-NHC complex did not isolated and used as formed for the synthesis of complex **6**. However, ^{1}H, ^{13}C and APT NMR spectra of in situ generated Ag(I)-NHC complex were recorded in order to understand in which step the oxidation of ligand takes place. The NMR spectra sign out that oxidation of pro-ligand occurs during the synthesis of silver-NHC complex due to a signal at 165.6 ppm which attributed to carbonil carbon of carboxylate group on the ^{13}C NMR spectra. In this light, the proposed structure for the in situ synthesised silver complex is shown in Figure 3. We think that carboxylate specie coordinates to silver centre due to ^{13}C NMR chemical shifts of carboxylate group on Ag(I)-NHC and complex **6** at 167,2 and 170, 6 ppm respectively. The NC_2N-Ag carben carbon peak was not detected probably due to low concentration or nature of silver-NHC complex.
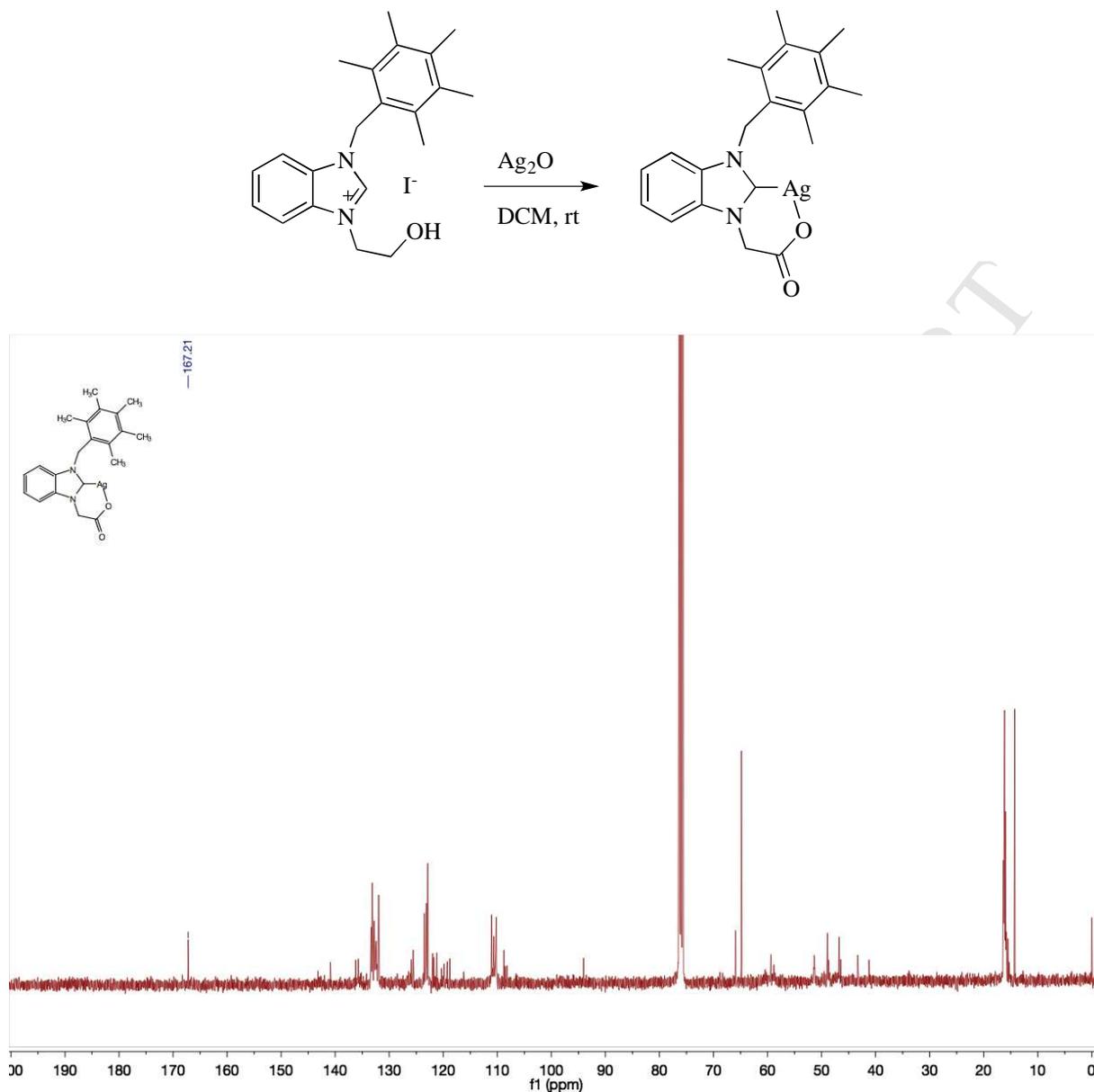
Figure 3. Proposed structure of in situ synthesised Ag(I)-NHC complex and ^{13}C NMR spectra

To synthesis complex **6**, 0.5 mmol RuCl$_2$(HMB)$_2$ was added to the DCM solution of Ag(I)-NHC in dark. After stirring 24 h at room temperature, reaction mixture was filtrated upon celite and all volatiles removed under high vacuum. By dissolving the crude product of **6** in DCM/diethyl ether solution led to obtain single crystals suitable for X ray diffractions analysis. The ^{1}H NMR of **6** in CDCl$_3$ confirms the formation of chelated Ru(II)-NHC complexes by evanescent NC*H*N proton. *C$_2$* carbon of chelated Ru(II)-NHC complexes in ^{13}C NMR spectra shifted to 191.5 ppm, also confirm formation of **6**. Also, CH$_2$COO-Ru carbon

resonate at 170.6 ppm which is the expected value (Figure 2). The APT NMR spectra of complex **6** confirming the formation of a *CH_2COO-* group by giving a peak in the negative zone at 170.6 ppm (Figure 2). The HRMS spectra were verified the proposed structures for the **6**, recorded in methanol in negative-ion mode. The most intense peaks correspond to molecular fragment ionized by the loss of one ion (Cl^-) in negative-ion mode. The HRMS spectra of complex **6** in methanol displayed ruthenium containing peaks.

2.2.Crystallography

The molecular structure of the complex **6** obtained from the ORTEP analysis of single crystal x-ray diffraction is given in Figure 4.
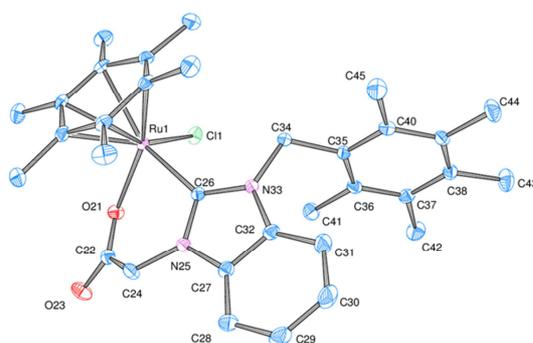
Figure 4. ORTEP plot of the complex **6**

The bond lengths (Å) and bond angles (^{o}) of the complex are shown in Table 1. The molecule structure of the complex was investigated by DFT calculations. The obtained crystallographic data, which included bonds lengths and the angles between atoms, is given in Table 1 and compared with the experimentally obtained crystallographic data. It can be seen that the computational and experimental crystallographic data were compatible with each other. For example, the experimental and computational bond lengths of Ru1-C26 and Ru1-O21 were 2.028-2.013 Å and 2.412-2.485 Å, respectively. The experimental and computational angles of N25-C26-Ru1 and N25-C26-N33 were 120.91^o-122.43^o and 105.88^o-105.92^o, respectively.

According to crystal structure of complex **6**, it can be said that the Ru(II) complex with an octahedral environment has a $t_{2g}^{6}e_{g}^{0}$ electronic configuration. It should be pointed out here that thermal spin state transition is not expected for the complex of 4d and 5d transition elements since the ligand field strength is very high when compared with similar 3d complexes. Hence, practically all 4d and 5d transition metal complexes show a low spin electronic configuration. The strength of the ligand fields was in order of 5d>4d>>3d [35]. Thus, a low spin configuration is expected in complex **6**, which was also support by the NMR results of the complexes.

Table 1 Analogy of experimental and theoretical computation bond length and angle results of the complex

Bond	Exp. Lenght (Å)	DFT Lenght (Å)
Ru1-Cl1	2.412	2.485
Ru1-O21	2.108	2.076
Ru1-C26	2.028	2.013
C26-N25	1.355	1.383
C26-N33	1.368	1.389
O21-C22	1.281	1.320
C22-O23	1.232	1.258
C22-C24	1.530	1.550
C24-N25	1.460	1.470
Ru1-C5	2.222	2.353
Ru1-C6	2.199	2.318
Ru1-C3	2.305	2.433
Ru1-C2	2.301	2.411
Angle	$(^{0})$	$(^{0})$
C4-Ru1-Cl1	92.19	91.58
C3-Ru1-Cl1	88.74	88.58
C5-Ru1-C26	93.30	99.97
C1-Ru1-O21	89.74	88.59
Ru1-O21-C22	125.57	126.60
O21-C22-O22	124.28	124.68
C22-C24-N25	115.86	116.53
C24-N25-C26	126.10	125.89
N25-C26-Ru1	120.91	122.43
C26-N33-C34	122.89	122.27
N25-C26-N33	105.88	105.92
O21-Ru1-C26	83.99	85.96
O21-Ru1-Cl1	84.77	86.55

Cl1-Ru1-C26	91.84	90.58
C26-N25-C27	111.20	110.85
C26-N33-C32	110.30	110.45
C1-C2-C3	119.77	119.62

2.3.HOMO and LUMO analysis

The electronic structure of complex **6** was calculated by the DFT computation technique from the optimised structure. Structural concordance was observed from the comparison of bond lengths and angles between the calculated and X-ray determined structure of **6**. The B3LYP/LanL2DZ basis set was used for the calculation of the energy of the highest occupied molecular orbital (HOMO) and the lowest unoccupied molecular orbital (LUMO). The energy of HOMO and LUMO orbitals were found to be -5.34186 eV and -1.454720 eV, respectively. The molecular energy gap (E_g = LUMO-HOMO) from the optimised molecular structure by DFT method was calculated as 3.88714 eV.

Figure 5b and c show the HOMO and LUMO states of the molecule, related to electrostatic interactions with the environment of **6**. Increasing the energy of the HOMO and decreasing the energy of the LUMO can cause a decrease in ionization energy. Due to the high energy gap value of **6**, it is expected that complex **6** is irrelevant to electron transfer.

(a)

(b)

(c)
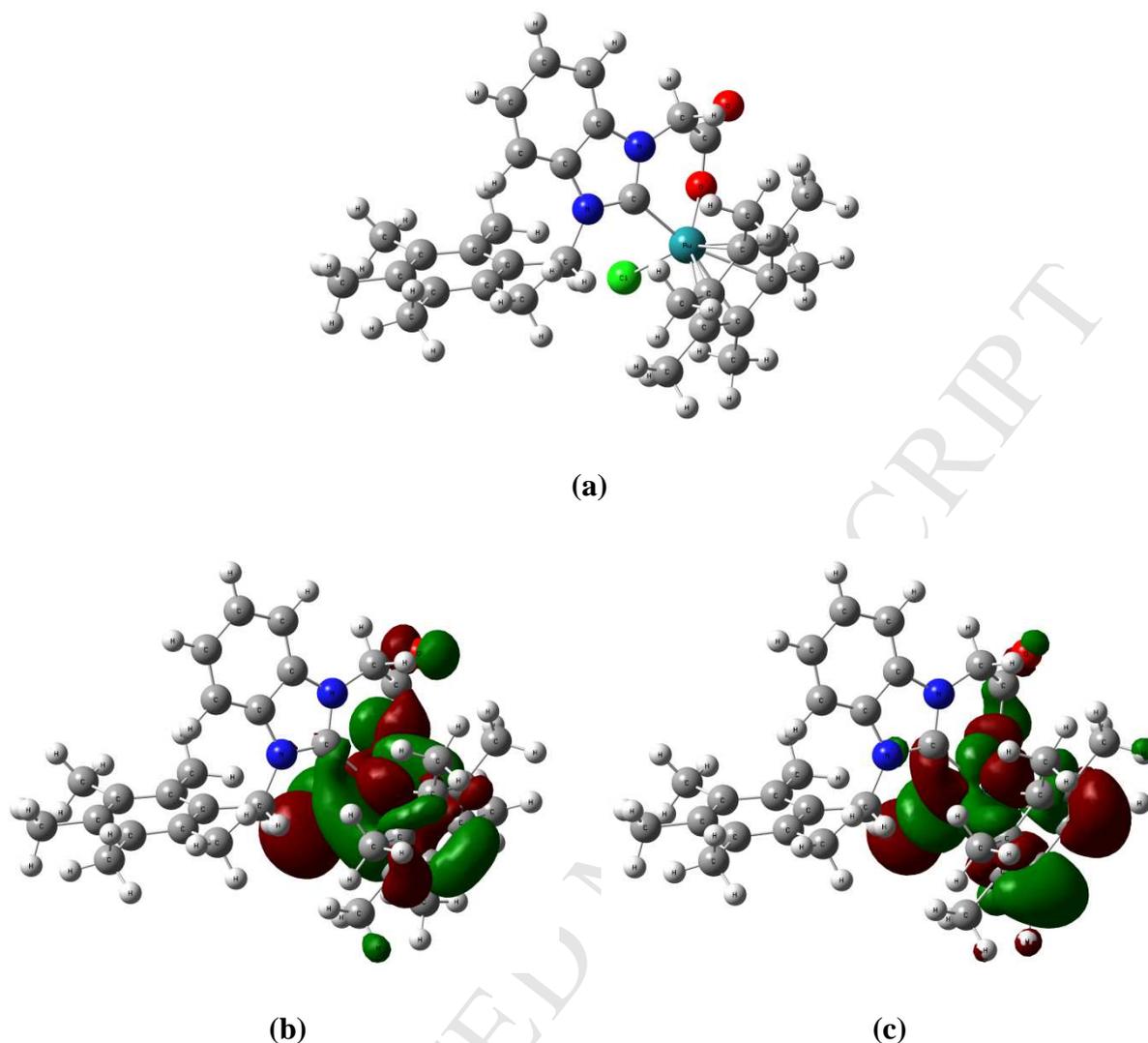
Figure 5. **(a)** Optimized molecule, **(b)** HOMO and **(c)** LUMO state by DFT calculation

The MEP results of the complex are given in Figure 6 and the green colored regions on correspond to positive electrostatic region and the red sink regions represent the negative electrostatic potential surface in the complex **6**. It is found that the value of the positively charged region is low when compared with the negatively charged region in Figure 6. So, it can be predicted that the complex has a nucleophilic character and is sensitive against electrophilic sort. It can be seen in Figure 6 that the electrophilic region of the complex has a small value, which means weak attractive potential for negative complexes, but the red region in Figure 6 shows a good electrophilic effect, especially in the region with Cl⁻ ions.
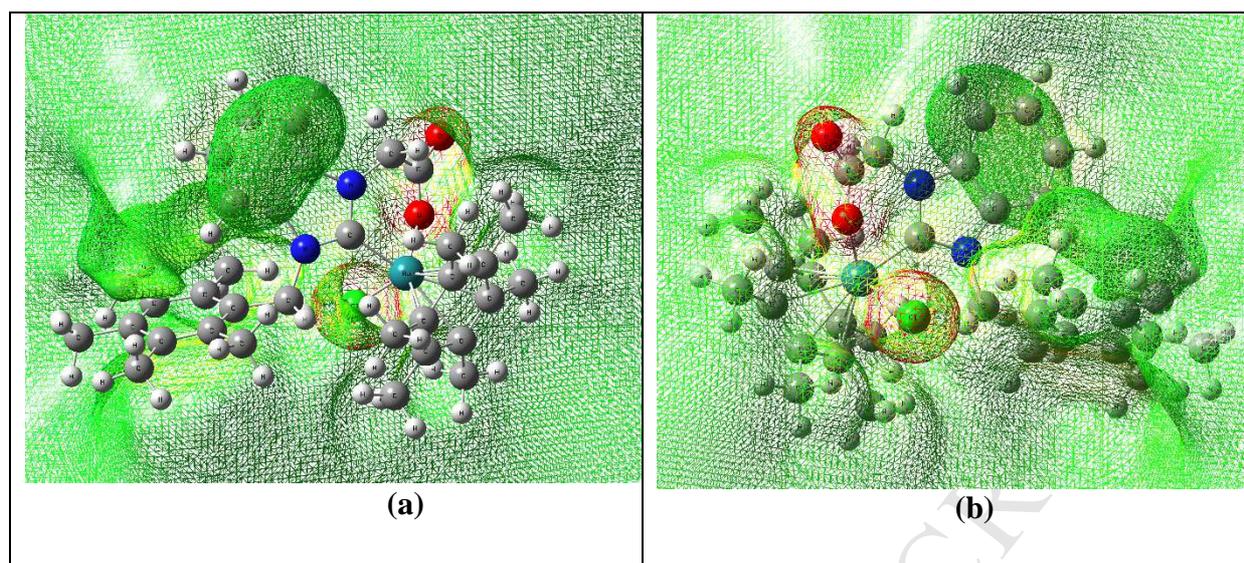
Figure 6. (a) front and (b) back view of MEP surface of the complex (green color indicates neutral charge density. The blue and red colors indicate the positive and negative charge densities, respectively)

2.4.Catalysis

The transfer hydrogenation reaction of ketones was conducted in refluxing 2-propanol using the ruthenium-based catalyst in the presence of a base; this is an important reaction in industry [36,37]. Under these conditions, stable catalysts are readily able to catalyse transfer hydrogenation reactions. The action of chelating donor-functionalised NHCs could be to stabilise the ruthenium centre while decomposition take place. The potency of chelating ruthenium NHC complexes as catalysts in the transfer hydrogenation reaction have been reported by different groups [9-12,38-42].

Table 2. Results of transfer hydrogenation of ketones catalyzed by complex **6**.

Ketone + OH $\xrightarrow[80\ ^oC]{\begin{array}{c}\text{[cat]}\\\text{KO}^t\text{Bu}\end{array}}$ Alcohol + O

Entry	Catalyst	Ketone	Product	Yield(%)[a]
1	6	O (cyclohexanone)	OH (cyclohexanol)	99
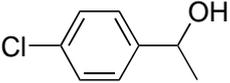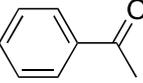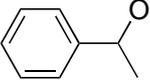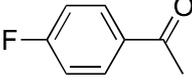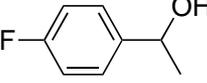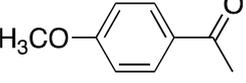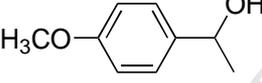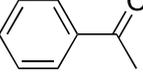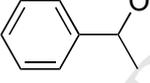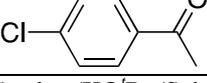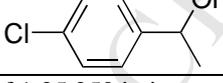
		Substrate	Product	Yield
2	6	Cl–C$_6$H$_4$–C(O)CH$_3$	Cl–C$_6$H$_4$–CH(OH)CH$_3$	98
3	6	C$_6$H$_5$–C(O)CH$_3$	C$_6$H$_5$–CH(OH)CH$_3$	95
4	6	F–C$_6$H$_4$–C(O)CH$_3$	F–C$_6$H$_4$–CH(OH)CH$_3$	60
5	6	H$_3$CO–C$_6$H$_4$–C(O)CH$_3$	H$_3$CO–C$_6$H$_4$–CH(OH)CH$_3$	45
6	none	C$_6$H$_5$–C(O)CH$_3$	C$_6$H$_5$–CH(OH)CH$_3$	3
7	none	Cl–C$_6$H$_4$–C(O)CH$_3$	Cl–C$_6$H$_4$–CH(OH)CH$_3$	8

All reactions were carried out with a Catalyst/KO^{t}Bu/Substrate ration of 1:25:250 in isopropanol (3 mL) at 80 ^{o}C in 2 hours under anhydrous and air free reaction conditions.

[a] Yields were determined by GC with undecane as internal standard and were reported as an average of three runs.

To our knowledge, there are no any reports on the transfer hydrogenation catalysed by ruthenium complexes with benzimidazole-based carboxylate-functionalised chelating NHCs. Complex **6** catalysed the transfer hydrogenation of ketones at 80 ^{o}C with 2-propanol as the hydrogen source in the presence of KO^{t}Bu as an activator (catalyst/base/substrate, 1:25:250; Table 2). With this loading under an air atmosphere, different ketones were turned into the corresponding alcohols with good to high yields in 2 hours.

2.5.Redox properties

Figure 7 shows the cyclic voltammograms taken in a 0.05 M acetonitrile solution of *n*-Bu$_4$NClO$_4$ as the supporting electrolyte containing 0.05 mM RuCl(NHC)(HMB). The curve shows the voltammogram obtained with the Pt working electrode and the Ag/AgO reference electrode.

Ruthenium complex **6** underwent a single-electron redox reaction between Ru(II) and Ru(III) in the activation/deactivation process, as illustrated in Figure 7. The measurement was carried out in acetonitrile at 25°C with *n*-Bu$_4$NClO$_4$ as the supporting electrolyte. Complexes showed

waves corresponding to the Ru(II) a Ru(III) interconversion, which was highly reproducible as quasi-reversible in each of several scans. The redox potential of complex **6** was E_{pa} = -0.13 V, E_{Pc} = 0.14 V, $E_{1/2}$ = 0.005 V for a 100 mV/s scan rate, as shown in Table 3. We concluded that low redox potential of complex **6** may help catalyse the transfer hydrogenation reaction. E_{Pc} and E_{pa} values changed with an increasing scan rate, which can be explained by the Randles-Sevcik equation showing that the peak values in CV are proportional to the square root of the scan rate.
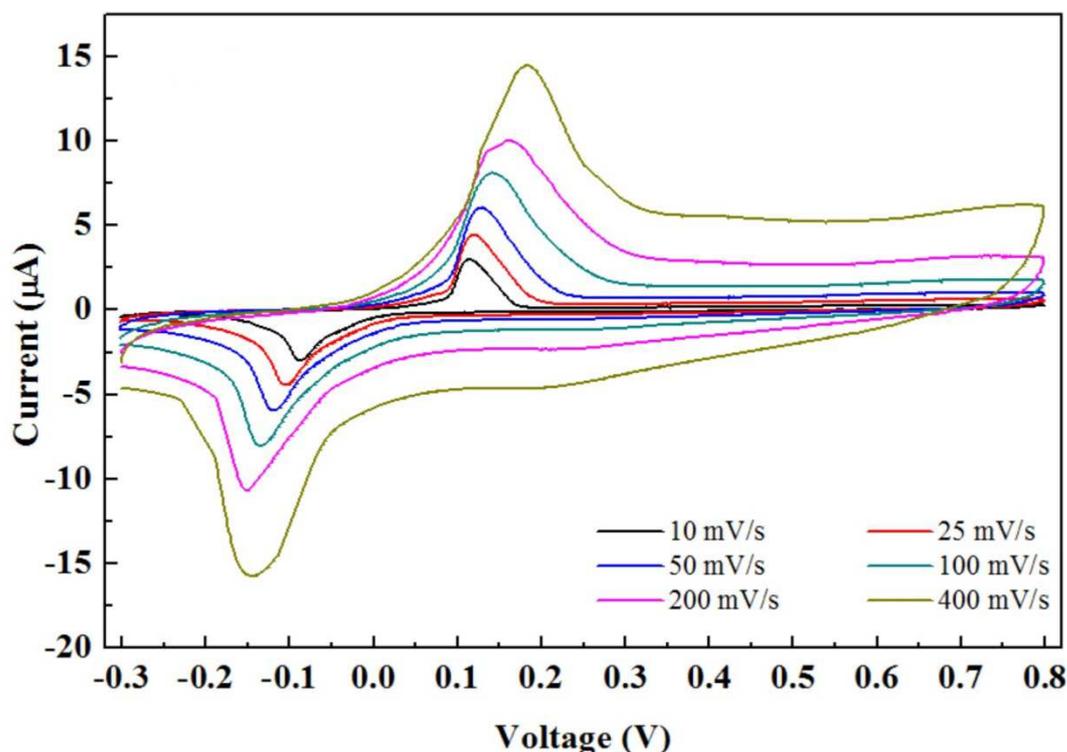

Figure 7. CV of the complex **6** for different scan rate

Table 3. CV properties of complex **6** on different scan rates

Scan Rates (mV/s)	E_{Pc} (eV)	E_{Pa}(eV)	$E_{1/2}$(eV)
400	0.18	-0.14	0.02
200	0.16	-0.14	0.01
100	0.14	-0.13	0.005

50	0.13	-0.12	0.005
25	0.12	-0.10	0.01
10	0.11	-0.08	0.02

2.6.Design of the hybrid capacitor and performance analysis

It was important to investigate the capacitive behavior of the complex. For this, we designed a device including an electrolyte and electrodes with the hybrid capacitor. To determine the cycle life and capacity of the device, fabricated using complex **6** as an electrode material, we fabricated a capacitor using a CR2032 coin cell case. The hybrid capacitors were designed in the electrode/electrolyte/membrane (cellulose)/electrolyte/electrode device configuration.
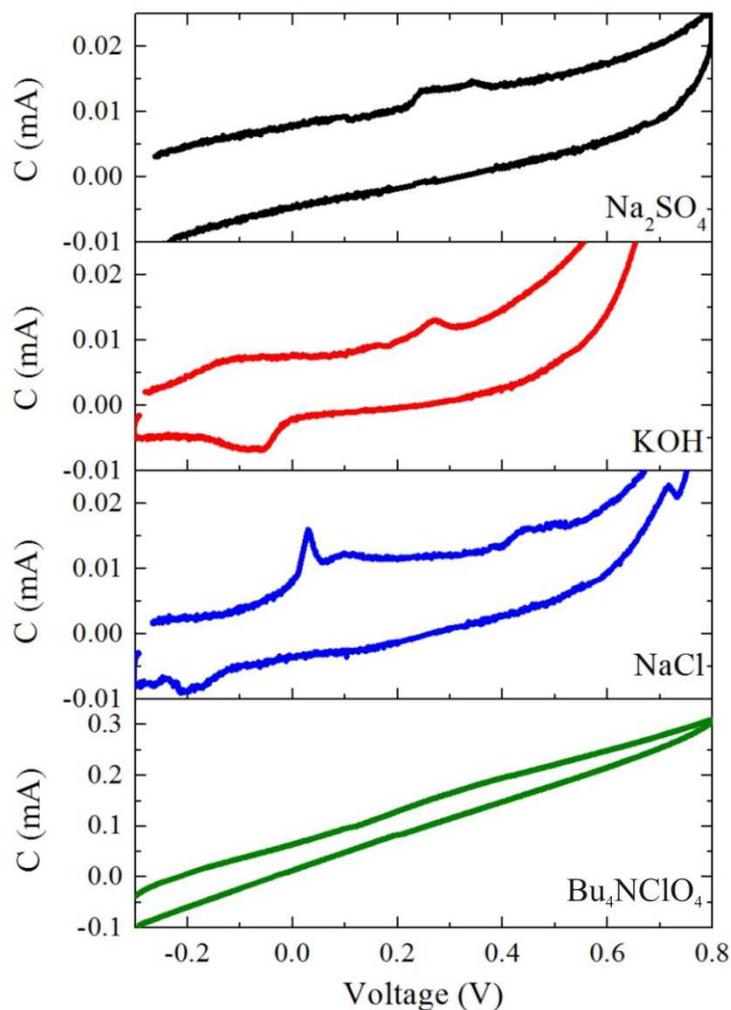
Figure 8. Cyclic Voltograms of complex **6** in different electrolytes

Although the CV graph of a supercapacitor is theoretically expected to have a rectangle shape, the CV graph of the hybrid capacitors exhibited a hysteretic curve with reduction and oxidation peaks, as seen in previous studies [43]. The oxidation and reduction peaks indicate a reversible reaction with the electrodes and electrolytes. It is well-known that the electrode and electrolyte interaction has an important effect on the capacitive properties. Thus, the interaction of positive and negative ions in the electrolyte is a key parameter of the CV graph of the cell. First of all, we measured the CV graph of the electrodes using four different electrolyte materials to determine the changes in the capacitive properties of the complex, as seen in Figure 8. Although all electrolytes showed a hysteretic structure during charge and

discharge of the cell, the electrolyte Bu_4NClO_4 showed the lowest performance for the capacitive properties and the electrolytes NaCl and Na_2SO_4 exhibited irreversible peaks during charge and discharge, which means surface modification of the electrodes occurred during the charge and discharge process. The best CV graph was obtained for the cell including the KOH electrolyte.

Figure 9a shows charge and discharge curve of the capacitors in the potential range of -0.3-0.8 V for different electrolytes. It can be seen that the charge curve shows an increase and the discharge curve exhibits an exponential decrease depending on the time, which is characteristic behaviour of a capacitor. A change in the electrolyte changed the time constant of the charge-discharge curve. It is well-known that the charging and discharging time is directly related to the capacity of the cell, and it can be seen in Figure 8a that the charging time is longer than discharging time, which is unwanted behaviour of the cell.

The capacity of the cell for different electrolyte materials was calculated by the following equation:

$$C = \frac{I}{-\frac{\Delta V}{\Delta t}} \cdot {1}/{m}$$

Where I is the applied constant current, which is positive for charging and negative for discharging, $\Delta V / \Delta t$ is the slope of the charge and discharge curve and m is the mass of the coated sample on the Ti substrate.

a)

b)
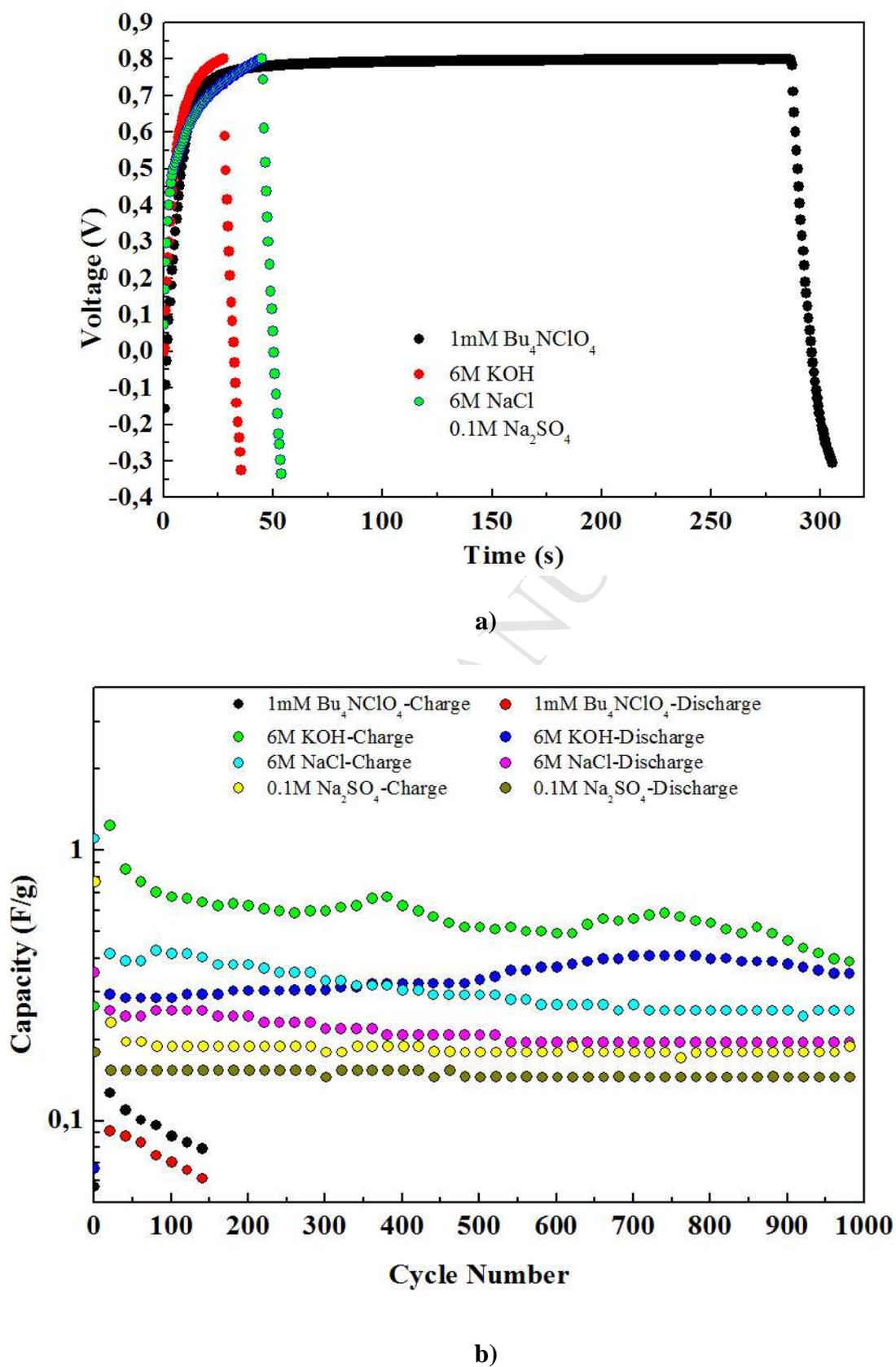
Figure 9. (**a**) Charge/discharge curve and (**b**) capacity-cycle number measurement of the cell for different electrolytes.

The capacity changes in the capacitors over 1000 cycles were measured, as seen in Figure 8b. Four different electrolyte materials were used to see the change in the capacity value of the cell. Figure 8b shows that the capacity of the cell fabricated using n-Bu$_4$NClO$_4$ was zero after 140 cycles of the cell and, when the cell was disassembled, we saw that the electrolyte was dried and it was concluded that the loss of capacitive behaviour of the cell was directly related with the drying of the electrolyte. When we compared the discharge capacity of the cell for different electrolytes, it was found that KOH>NaCl>Na$_2$SO$_4$. This needs further intensive study to develop higher capacity cells.

Table 4. The capacity of the cell for charging (Ch), discharging (Dch) and capacity fade (C.F) of the cells fabricated using different electrolytes

Electrolyte	1st Cycle		100th Cycle			250th Cycle			500th Cycle			1000th Cycle		
	Ch.	Dch.	Ch.	Dch.	C.F	Ch.	Dch.	C.F	Ch.	Dch.	C.F	Ch.	Dch.	C.F
	(Fg^{-1})		(Fg^{-1})		%	(Fg^{-1})		%	(Fg^{-1})		%	(Fg^{-1})		%
Bu$_4$NClO$_4$	0.28	0.12	0.08	0.07	50	-	-		-	-		-	-	
KOH	20.2	0.36	0.67	0.28	12	0.59	0.3	6	0.52	0.33	3	0.38	0.35	1
NaCl	1.11	0.35	0.40	0.25	14	0.35	0.23	12	0.29	0.21	14	0.24	0.19	16
Na$_2$SO$_4$	0.76	0.17	0.18	0.15	2	0.18	0.15	2	0.18	0.15	2	0.18	0.15	2

The charge/discharge capacity at the first, 100th, 250th, 500th and 1000th cycle and the capacity fade values of the cell for different electrolytes are presented in Table 4.

The first capacity value of the cell with KOH showed 20.2 Fg^{-1}, which is close to the capacity value of a traditional supercapacitor cell [44]. It was concluded that the complex 6 has excellent potential in supercapacitor applications, and we believe that these organometallic compounds will be used as supercapacitors in the near future after improving their properties.

The explanation of the fast decrease on the capacity of the cell is an important for future studies. The decrease may be related to the reactions with the electrolyte (the K^+ and OH^- ions for KOH) and complex **6** which causes to obstruct the formation of electric field. Another factor may be given the formation of buffer layer which block the formation of uniform electric field due to motion of ions in electrolyte component. The last possible mechanism may be the loss of the ionic permeability of the membrane. As a result, the fast capacity fade of the cell should be pointed out some in situ experiments during the cycling of the cell.

3. Conclusions

In this study, we successfully synthesized complex **6** and the crystal structure data was compared with experimentally obtained and theoretically calculated data from the Gaussian program. It was found that the structure matched the theoretically calculated data. The energy gap of HOMO and LUMO of complex **6** was 3.88714 eV, which is important for the catalytic activity.

We used complex **6** as a hybrid capacitor cell by using as an electrode material. Different electrolyte materials were used to determine the highest performance of the cell. It should be noted that KOH as an electrolyte in the cell was the best capacitive performance among the others in this study. The highest obtained capacity value of complex **6** was 20.2 F/g, which is a promising result for the energy storage applications for organometallic compounds. For

energy technology, the capacitive properties of Ru-complexes is important, and we believe that this type compound will be used as an energy storage material in the near future.

4. Experimental Section

4.1. General procedures

The ^{1}H and ^{13}C NMR spectra were recorded with a Bruker Avance III 300 or 400 MHz NMR spectrometer with sample solutions prepared in $CDCl_3$. The chemical shifts were reported in δ units downfield from the internal reference (Me_4Si) as seen in Figure 2. ($C_{33}H_{41}ClN_2O_2Ru$); M= 634.20. D8 VENTURE Bruker AXS diffractometer *, Mo-K_α radiation ($\lambda = 0.71073$ Å), T = 150 K; triclinic P -1 (I.T.#2), a = 8.7163(7), b = 11.0249(10), c = 17.5312(15) Å, $\alpha =$ 81.993(3), $\beta = 87.738(3)$, $\gamma = 83.814(3)$ °, V = 1658.0(2) Å3. Z = 2, d = 1.270 g.cm-3, $\mu =$ 0.582 mm^{-1}. The structure was solved by a dual-space algorithm using the SHELXT program [45], and then refined with the full-matrix least-squares methods based on F2 (SHELXL) [46]. The contribution of the disordered solvents to the calculated structure factors was estimated following the BYPASS algorithm [47], implemented as the SQUEEZE option in PLATON [48]. A new data set, free of the solvent contribution, was then used in the final refinement. All non-hydrogen atoms were refined with anisotropic atomic displacement parameters. H atoms were finally included in their calculated positions and treated as riding on their parent atom with constrained thermal parameters. A final refinement on F2 with 7599 unique intensities and 359 parameters converged at $\omega R(F2) = 0.0546$ (R(F) = 0.0227) for 6958 observed reflections with I > 2σ(I). The ORTEP plot of the crystal structure is given in supporting info.

Cyclic voltammetry of **6** was performed by using Zive SP1 potentiostat/galvanostat. A three-electrode electrochemical cell system was used for CV measurements and the Ag/AgCl electrode was chosen as the reference, a platinum disk as the working electrode and a

platinum wire in the as the counter electrode were used in the cell, with acetonitrile containing tetrabutylammoniumperchlorate (TBAP) as the supporting electrolyte. Electrochemical grade TBAP and acetonitrile were purchased from Sigma-Aldrich. The CV of **6** was studied in the potential range of +0.8 to -0.3 V at a differential scan rate of 10-400 mV/s.

To perform a device of the hybrid-capacitor, the following procedure was used. Before the film application, the mixture of 80% complex **6**, 10% carbon black and 10% PVDF were milled in an ball milling system for 2h then an appropriate amount of NMP was added to powder and re-milled for 24h. The obtained gel form of the mixture were coated on the Ti foil using 100 µm doctor blade and were dried at 100^oC for evaporation of the solvent. The film was cut for 1.5 cm diameters for the insertion of the CR2032 case. Since the anode and cathode of the capacitor are same, we named as electrode for both component of the cell. Na_2SO_4, KOH, NaCl and n-Bu_4NClO_4 were used as electrolyte materials for the cells. The hybrid capacitors were designed as electrode /electrolyte/membrane (cellulose)/electrolyte /electrode configuration for device fabrication. The CV measurement of the cell was performed using a two-electrode configuration and the capacity was measured using a constant current of ±1 mA for the voltage range of (-0.4)-(+0.8) V since the largest loop was obtained for this range in the CV graph of the cells.

The hybrid capacitors were designed using a CR2032 coin cell case and the electrode /electrolyte/membrane (cellulose)/electrolyte /electrode configuration was used for device fabrication. The electrode materials were coated on Ti foil 8 mm in diameter using a doctor blade. The film was fabricated using 80% active material, 10% carbon black and 10% PVDF to increase conductivity and the grip of the electrode materials on the Ti substrate. Na_2SO_4, KOH, NaCl and n-Bu_4NClO_4 were used as electrolyte materials for the cells. The CV measurement of the cell was performed using a two-electrode configuration and the capacity was measured using a constant current of ±1 mA.

DFT optimisations of complex **6** were performed using the GAUSSIAN 09 W software package with the B3LYP (Becke, 3-parameter, Lee-Yang-Parr)/LanL2DZ (Los Alamos National Laboratory 2 Double Zeta) basis set. First, the molecular geometry was optimised by DFT to determine the global minimum energy level and the optimised structure. The excited level, HOMO and LUMO energies and molecular electrostatic potential (MEP) of complex **6** were obtained by these calculations. GC analyses were performed on a Shimadzu GC-2010 Plus equipped with an HP-5 capillary column. The yields were calculated by GC using an internal standard (undecane); the yields are based on ketones.

4.2. Synthesis

4.2.1. 1-pentamethylbenzyl-3-hydroxyethylbenzimidazolium iodide

1-(pentamethylbenzyl)benzimidazole (1 mmol) was dissolved in *n*-BuOH (5 mL), then 2-hydroxyethyl iodide (1.2 mmol) was added. The solution was stirred for 24 h at 120°C. The precipitated yellow solid was filtered, washed with diethyl ether (3x5 mL) and dried under high vacuum. The precipitate was then crystallised from DCM-diethyl ether to give the title compound as a yellow crystal (0.35 g, 75%).

^{1}H NMR (400 MHz, CDCl$_3$) δ = 8.97 (s, 1H, NC*H*N), 7.80-7.50 (m, 4H, C$_6$*H$_4$*), 5.59 (s, 4H, C*H$_2$*C$_6$(CH$_3$)$_5$-2,3,4,5,6), 4,64 (t, *J*=8 Hz, 4H, NC*H$_2$*CH$_2$), 3.95 (t, *J*=8 Hz, 4H, NCH$_2$C*H$_2$*), 2.32 and 2.29 (s, 15H, CH$_2$C$_6$(C*H$_3$*)$_5$-2,3,4,5,6).^{13}C NMR (100 MHz, CDCl$_3$) δ = 140.7, 137.9, 134.3, 133.6, 132.0, 131.6, 127.5, 127.4, 124.1, 113.6, 113.2, 58.7, 49.9, 47.4, 17.4, 17.3, 17.2, 17.1, 17.0.

4.2.2. Synthesis of complex **6**

A suspension of 1-pentamethylbenzyl-3-hydroxyethylbenzimidazolium iodide (1 mmol) and Ag$_2$O (1 mmol) was added to 10 mL of ad DCM, placed in a Schlenk tube and stirred in the dark for 5 hours. Then, 0.5 mmol RuCl$_2$(HMB)$_2$ was added to the solution. After stirring in

the dark for 24 hours, the crude product was filtered through a pad of Celite in air. The filtrate was concentrated to 5 mL and 10 mL of hexane was added to afford complex **6** as orange crystals (0.4 g, 63%).

^{1}H NMR (CDCl$_3$, 400 MHz, 25 ^{o}C): δ=1.98 (s, 3H, CH$_2$C$_6$(C*H$_3$*)$_5$), 2.10 (s, 18H, C$_6$(C*H$_3$*)$_6$), 2.26 (s, 6H, CH$_2$C$_6$(C*H$_3$*)$_5$), 2.33 (s, 3H, CH$_2$C$_6$(C*H$_3$*)$_5$), 4.32 (d, 1H, *j* = 20 Hz, C*H$_2$*COO), 4.93 (d, 1H, *j* = 20 Hz, C*H$_2$*COO), 5.37 (d, 1H, *j* = 20 Hz, C*H$_2$*C$_6$(CH$_3$)$_5$), 5.93 (d, 1H, *j* = 20 Hz, C*H$_2$*C$_6$(CH$_3$)$_5$), 6.45 (d, 1H, *j* = 20 Hz, C$_6$*H$_4$*), 6.73 (t, 1H, *j* = 12 Hz, C$_6$*H$_4$*), 7.03 (t, 1H, *j* = 12 Hz, C$_6$*H$_4$*), 7.19 (d, 1H, *j* = 20 Hz, C$_6$*H$_4$*). ^{13}C NMR (CDCl$_3$, 100 MHz, 25 ^{o}C):δ=16.3 (C$_6$(*C*H$_3$)$_6$), 16.7, 17.1, 17.3, 17.5, 17.7 (CH$_2$C$_6$(*C*H$_3$)$_5$), 49.7 (*C*H$_2$COO), 50.4 (*C*H$_2$C$_6$(CH$_3$)$_5$), 94.7 (*C$_6$*(CH$_3$)$_6$), 109.1, 111.5, 122.4, 122.9 (*C$_6$*H$_4$), 128.1, 132.5, 133.3, 133.8, 34.4, 135.2, 136.2, 136.9 (CH$_2$*C$_6$*(CH$_3$)$_5$), 170.6 (CH$_2$*C*OO), 191.5 (*C$_2$*-Ru). HRMS (ESI): calcd. for C$_{33}$H$_{41}$ClN$_2$O$_2$Ru [M-H]$^-$ 635.1978; found 635.1970; calcd. for C$_{33}$H$_{41}$N$_2$O$_2$Ru [M-Cl]$^-$ 599.2212; found 599.2230.

Appendix A. Supplementary data

CCDC 1579884 contains the supplementary crystallographic data for the compound reported in this article. These data can be obtained free of charge via http://www.ccdc.cam.ac.uk/data_request/cif, or from the Cambridge Crystallographic Data Centre, 12 Union Road, Cambridge CB2 1EZ, UK; fax: (+44) 1223-336-033; or e-mail: deposit@ccdc.cam.ac.uk.

REFERENCES

[1] (a) From Laboratory Curiosities to Efficient Synthetic Tools, RSC Publishing, Cambridge, UK, 2011; (b) F. Glorius, N-Heterocyclic Carbenes in Transition Metal Catalysis, Springer-Verlag, Heidelberg, Germany, 2007; (c) V. Ceśar, S. Bellemin-Laponnaz, L. H. Gade, Chem. Soc. Rev. 33 (2004) 619 ; (d) F. E. Hahn, M. C. Jahnke, Angew. Chem. Int. Ed. 47 (2008) 3122; (e) S. Dı́ez-Gonzaĺez, N. Marion, S.P. Nolan, Chem. Rev. 109 (2009) 3612; (f) J. C. Y.Lin, R.T.W. Huang, C.S. Lee, A.W. Bhattacharyya, S. Hwang, I. J. B. Lin, Chem. Rev. 109 (2009) 3561; (g) P. L. Arnold, I. J. Casely, Chem. Rev. 109 (2009) 3599.

[2] (a) D. Enders, O. Niemeier, A. Henseler, Chem. Rev. 107 (2007) 5606; (b) N. Marion, S. Dı́ez-Gonzaĺez, S.P. Nolan, Angew. Chem. Int. Ed. 46(2007) 2988.

[3] (a) G. Gasser, I. Ott, N. Metzler-Nolte, J. Med. Chem. 54 (2011) 3; (b) K. A. Nebioglu, M. J. Panzner, C.A. Tessier, C.L. Cannon, W. Youngs, J. Coord. Chem. Rev. 251 (2007) 884.

[4] W. A. Herrmann, Angew. Chem. Int. Ed. 41 (2002) 1290–1309

[5] (a) Lee, H. M.; Lee, C. C.; Cheng, P. Y. Curr. Org. Chem. 2007, 11, 1491; (b) O. Kuhl, Chem. Soc. Rev. 36 (2007) 592; (c) A. John, P. Ghosh, Dalton Trans. 39 (2010) 7183

[6] (a) M. Bierenstiel, E.D. Cross, Coord. Chem. Rev. 255 (2011) 574; (b) C. Fliedel, P. Braunstein, Organometallics, 29 (2010) 5614; (c) C. Fliedel, A. Sabbatini, P. Braunstein,

Dalton Trans. 39 (2010) 8820; (d) C. Fliedel, G. Schnee, P. Braunstein, Dalton Trans. 2474 (2009) 2474; (e) A. Ros, M. Alcarazo, D. Monge, E. Alvarez, R. Ferna ́ndez, J. M. Lassaletta, Tetrahedron Asymmetry, 21 (2010) 1557; (f) S. J. Roseblade, A. Ros, D. Monge, M. Alcarazo, E. Alvarez, J.M. Lassaletta, R. Fernandez, Organometallics, 26 (2007) 2570; (g) A. Ros, D. Monge, M. Alcarazo, E. Alvarez, J.M. Lassaletta, R. Fernandez, Organometallics, 25 (2006) 6039; (h) H. V. Huynh, D. Yuan, Y. Han, Dalton Trans. (2009), 7262; (i) H.V. Huynh, C.H. Yeo, G.K. Tan, Chem. Commun. (2006) 3833

[7] C. Gandolfi, M. Heckenroth, A. Neels, G. Laurenczy, M. Albrecht, Organometallics, 28 (2009) 5112

[8] A. T. Normand, K.J. Cavell, Eur. J. Inorg. Chem. (2008) 2781–2800.

[9] S. Horn, C. Gandolfi, M. Albrecht, Eur. J. Inorg. Chem. 2011, 2863–2868.

[10] J. DePasquale, J.; N.J. White, E.J. Ennis, M. Zeller, J.P. Foley, E.T. Papish, Polyhedron, 58 (2013) 162–170.

[11] P.L. Chiu, H.M. Lee, Organometallics, 24 (2005) 1692–1702.

[12] V. Miranda-Soto, D.B. Grotjahn, A.L. Cooksy, J.A. Golen, C.E. Moore, A.L. Rheingold, Angew. Chem. Int. Ed. 2011, 50, 631–635.

[13] (a) J. Huang, E. D. Stevens, S.P. Nolan, J.L. Petersen, J. Am. Chem. Soc., 121 (1999) 2674; (b) M. Poyatos, M. Mas-Marza, M. Sanau, E. Peris, Inorg. Chem. 43 (2004) 1793; (c) L. Mercs, A. Neels, M. Albrecht, Dalton Trans. (2008) 5570; (d) Y. Cheng, H-J. Xu, J-F. Sun, Y-Z. Li, X-T. Chen, Z-L. Xue, Dalton Trans., (2009) 7132.

[14] A. Labande, J-C. Daran, N.J. Long, A.J.P. White, R. Poli, New J. Chem., 35 (2011) 2162–2168.

[15] Y. Cheng, J-F. Sun, H-L. Yang, H-J. Xu, Y-Z. Li, X-T. Chen, Z-L. Xue, Organometallics, 28 (2009) 819–823.

[16] W. B. Cross, C. G. Daly, Y. Boutadla, K. Singh, Dalton Trans. 40 (2011) 9722–9730

[17] W. N. O. Wylie, A. J. Lough, R.H. Morris, Chem. Commun.46(2010) 8240–8242.

[18] F. Zeng, Z. Yu, Organometallics, 27 (2008) 6025–6028.

[19] A. Sinha, P. Daw, S. M. W. Rahaman, B. Saha, J.K. Bera, J. Organomet. Chem.,696 (2011) 1248–1257.

[20] W. N. O. Wylie, A.J. Lough, J. H. Morris, Organometallics, 28 (2009) 6755–6761.

[21] M. Poyatos, J. A. Mata, E. Falomir, R. H. Crabtree, E. Peris, Organometallics, 22 (2003) 1110–1114.

[22] M. Poyatos, A. Maisse-François, S. Bellemin-Laponnaz, E. Peris, L.H. Gade, J. Organomet. Chem., 691 (2006) 2713–2720.

[23] F. E. Fernández, M. C. Puerta, P. Valerga, Organometallics, 30 (2011) 5793–5802.

[24] F. E. Fernández, M. C. Puerta, P. Valerga, Organometallics, 31 (2011) 6868–6879.

[25] X-W. Li, F. Chen, W-F. Xu, Y-Z. Li, X-T. Chen, Z-L. Xue, Inorg. Chem. Commun. 14 (2011) 1673–1676.

[26] W. N. O. Wylie, A. J. Lough, R.H. Morris, Organometallics, 30 (2011) 1236–1252.

[27] M. Benitez, E. Mas-Marza, J. A. Mata, E. Peris, Chem. Eur. J. 17 (2011) 10453.

[28] P. N. Muskawar, P. Karthikeyan, S. A. Aswar, P. R. Bhagat, S. S. Kumar, Arab. J. Chem. 9 (2016) 1765-1778.

[29] S. Hong, S. H. Lee, S. W. Kim, Electrochem. Solid-State Lett. 5 (2002) 227-230.

[30] V. Barranco, M. A. Lillo-Rodenas, A. Linares-Solano, A. Oya, F. Pico, J. Ibañez, F. Agullo-Rueda, J. M. Amarilla, J. M. Rojo, J. Phys. Chem. C, 114 (2010) 10302–10307.

[31] T. Chen, L. Dai, Materials Today, 16 (2013) 272-280.

[32] (a) Q.Yang, Z. Lu, J. Liu, X. Lei, Z. Chang, L. Luo, X. Sun, Natural Science: Materials International, 23 (2013) 351-366; (b) D-Y. Lee, G-H. An, H-J. Ahn, journal of Industrial and Engineering Chemistry, 52 (2017) 121-127; (c) J. Bae, J. Y. Park, O. S. Kwon, C-S. Lee, Journal of Industrial and Engineering Chemistry, 51 (2017) 1-11; (d) H. R. Barai, A. N. Banerjee, F. Bai, S. W. Joo, Journal of Industrial and Engineering Chemistry, article in press, 2018.

[33] J-Y. Wang, M-C. Wang, D-J. Jan, Sol. Energy Mater Sol. Cells. 160 (2017) 476-483.

[34] C. Zhong, Y. Deng, W. Hu, J. Qiao, L. Zhang, J. Zhang, Chem. Soc. Rev. 44 (2015) 7484.

[35] M. M. T. Khan, Activation Of Small Inorganic Molecules, 1st Edition, Elsevier, 2012.

[36] A. J. Blacker, Enantioselective transfer hydrogenation, in: C.J.E. Johannes, G. De Vries (Eds.), The handbook of homegenous hydrogenation, Wiley-VCH, Weinheim, 2007.

[37] T. Ikariya, A. J. Blacker, Acc. Chem. Res. 40 (2007) 1300-1308.

[38] W. Baratta, J. Schütz, E. Herdtweck, W.A. Herrmann, P. Rigo, J. Organomet. Chem., 690 (2005) 5570–5575.

[39] S. Burling, B.M. Paine, D. Nama, W.S. Brown, M.F. Mahon, T.J. Prior, P.S. Pregosin, M.K. Whittlesey, J. M .J . Williams, J. Am. Chem. Soc., 129 (2007) 1987–1995.

[40] N. Gürbüz, S. Yaşar, E.Ö. Özcan, İ. Özdemir, B. Çetinkaya, Eur. J. Inorg. Chem. 19 (2010) 3051–3056.

[41] S. Demir, İ. Özdemir, B. Çetinkaya, E. Sahin, C. Arici, J. Coord. Chem. 64 (2011) 2565–2572.

[42] B. Yigit, M. Yigit, I. Özdemir, E. Çetinkaya, Transit. Met. Chem. 37 (2012) 297–302.

[43] J. Ajuria, E. Redondo, M. Arnaiz, R. Mysyk, T. Rojo, E. Goikolea, J. Power Sources, 359 (2017) 359, 17-26.

[44] X. Zhang, X. Wang, L. Jiang, H. Wu, H. Wu J. Su, J. Power Sources, 216 (2012) 290-296.

[45] G. M. Sheldrick, Acta Cryst. A71 (2015) 3-8.

[46] G.M. Sheldrick, Acta Cryst. C71 (2015) 3-8.

[47] P. V. D. Sluis, A. L. Spek, Acta Cryst. A46 (1990) 194-201.

[48] A. L. Spek, J. Appl. Cryst. 36 (2003) 7-13.

Highlights:

- Benzimidazol based NHC ligand and its chelated Ru(II)-NHC complex was reported.

- Structure for Ag(I)-NHC was proposed.

- Hybrid capacitor potential of chelated Ru(II)-NHC complex was investigated and reported for the first time.